Visualization of a Unidirectional Electromagnetic Waveguide Using Topological Photonic Crystals Made of Dielectric Materials

Yuting Yang,[1] Yun Fei Xu,[1] Tao Xu,[1] Hai-Xiao Wang,[1] Jian-Hua Jiang,[1] Xiao Hu,[2,*] and Zhi Hong Hang[1,3,†]
[1]College of Physics, Optoelectronics and Energy and Collaborative Innovation Center of Suzhou Nano Science and Technology, Soochow University, Suzhou 215006, China
[2]International Center for Materials Nanoarchitectonics (WPI-MANA), National Institute for Materials Science, Tsukuba 305-0044, Japan
[3]Key Laboratory of Modern Optical Technologies (Soochow University), Ministry of Education and Key Lab of Advanced Optical Manufacturing Technologies of Jiangsu Province, Suzhou 215006, China

(Received 13 November 2017; published 22 May 2018)

We demonstrate experimentally that a photonic crystal made of Al_2O_3 cylinders exhibits topological time-reversal symmetric electromagnetic propagation, similar to the quantum spin Hall effect in electronic systems. A pseudospin degree of freedom in the electromagnetic system representing different states of orbital angular momentum arises due to a deformation of the photonic crystal from the ideal honeycomb lattice. It serves as the photonic analogue to the electronic Kramers pair. We visualized qualitatively and measured quantitatively that microwaves of a specific pseudospin propagate only in one direction along the interface between a topological photonic crystal and a trivial one. As only a conventional dielectric material is used and only local real-space manipulations are required, our scheme can be extended to visible light to inspire many future applications in the field of photonics and beyond.

DOI: 10.1103/PhysRevLett.120.217401

Introduction.—The introduction of topology unravels a new chapter of physics [1–3]. Topological systems provide unique edge or interface quantum states, which are expected to contribute to the development of spintronics and quantum computation [4–9]. Photonic systems can also benefit from topology. By paralleling Maxwell's equations for electromagnetic (EM) waves and Schrödinger's equation for electrons, Haldane and Raghu [10] showed that chiral edge states can be realized for EM waves. The prediction was confirmed experimentally using gyromagnetic materials under an external magnetic field [11–13] and helical optical fibers with light injection [14]. Topologically protected EM propagation with time-reversal symmetry (TRS) is preferred as being more compatible with established semiconductor technology. However, when TRS is preserved, the difference between EM waves and electronic systems becomes more significant. Kramers degeneracy is a concept referring to the doubly degenerate energy states intrinsically related to fermions with half-integer spin angular momentum when TRS is present [15]. The Kramers pair formed by the up- and down-spin states is crucial for the realization of the electronic helical edge states in quantum spin Hall effect (QSHE) systems [4–8]. Photons, quantized EM waves, obey the Bose-Einstein statistics for which no intrinsic Kramers pairing can be expected. Recent effort has been devoted to the creation of TRS topological EM propagation [16] using a variety of ways to mimic Kramers pairing in bosonic systems. Among others, bianisotropic materials [17,18], coupled resonator waveguides [19,20], structures with engineered synthetic gauge fields [21–23], and waveguides with broken mode symmetry [24,25] have been proposed and experimentally realized.

Photonic crystals (PCs) are the analogue of electronic crystals in which the periodic atomic potential is replaced by a periodic distribution of permittivity and/or permeability [26]. In contrast to atomic crystals, the use of engineered "artificial molecules" in PCs enables the creation of a rich variety of topological photonic states not easily accessible in natural systems. As an example, a scheme was proposed to realize two-dimensional (2D) topological states with TRS by exploring the C_{6v} symmetry [27], and related topological phenomena were then observed experimentally in an acoustic system with steel rods [28] and in an EM system with metallic rods [29]. We notice that up to this moment the demonstration of topological EM propagation in PCs made of dielectric materials is lacking. However, such a demonstration is of special importance, since the realization of topological EM features in visible light for which the element sizes will be scaled down [14,27,30,31] has been hampered by the lack of suitable gyromagnetic materials and by high losses in metallic structures.

In this Letter, we engineer experimentally a honeycomb PC of alumina cylinders, a conventional dielectric material, to create a pair of photonic pseudospin states mimicking the electronic Kramers pair and to induce a topological phase transition in a TRS system. EM waves of a desired pseudospin state are excited by a designed antenna array.

We demonstrate successfully their unidirectional propagation in microwave channels, where the topologically protected EM transportation is proven both by visualizing qualitatively the pathway along the interface between topological and trivial PCs and by measuring quantitatively the energy flow along the interface. The EM properties demonstrated explicitly here are readily transferrable to near-infrared and even optical wavelengths, which are expected to be able to contribute to future optical science and technology.

Design of the system.—We consider triangular lattices of artificial molecules formed by six dielectric cylinders [see Fig. 1(a) and Supplemental Material [32] Sec. I]. Here, we consider the transverse magnetic (TM) mode with out-of-plane electric field and in-plane magnetic field. As schematically shown in Fig. 1(b), there are two competing lengths in such a composite lattice: the intracouple distance h_1, defined as the distance between neighboring cylinders within a same molecule, and the intercouple distance h_2, defined as the distance between the nearest cylinders in the neighboring molecules, with $2h_1 + h_2 = a$ giving the lattice constant of the triangular lattice. For $h_1 \neq h_2$, a frequency gap opens in the frequency dispersion as shown in Fig. 1(c), and dipolar (E_1) and quadrupolar (E_2) EM

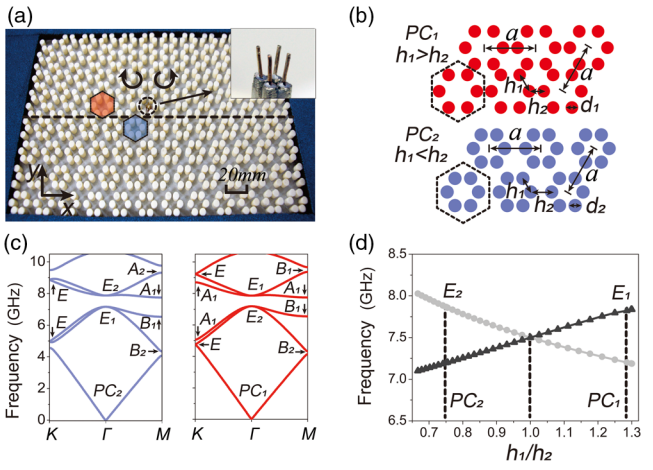

FIG. 1. (a) Photo of the experimental setup to realize EM pseudospin states and a unidirectional photonic channel, where two photonic crystals PC_1 and PC_2 are assembled in the regions above and below the interface (dashed line). A square-shaped antenna array (dashed circle near the interface and enlarged in the inset) is used to selectively excite one of the two EM pseudospin states indicated by circular arrows. The sample is located inside a parallel-plate waveguide with the top metallic plate removed in the photo. (b) Schematics of PC_1 in dark gray (red online) and PC_2 in gray (blue online) as characterized by two competing lengths h_1 and h_2. (c) Calculated bulk TM photonic band diagrams of PC_1 (right) and PC_2 (left), with the corresponding 2D representations of eigenmodes at high-symmetry points labeled. (d) Upon increasing the ratio between h_1 and h_2, the frequencies of the doubly degenerate $E_1(E_2)$ modes increase (decrease), and a band inversion occurs when $h_1/h_2 = 1$.

modes appear at the two band edges at the Γ point, the center of the Brillouin zone (BZ). They are associated with the 2D representations E_1 and E_2 of the C_{6v} point group, whose mode profiles are isomorphic to the p_x/p_y orbitals and $d_{x^2-y^2}/d_{xy}$ orbitals, respectively [38]. Their linear combinations $|p_\pm\rangle = |p_x\rangle \pm i|p_y\rangle$ and $|d_\pm\rangle = |d_{x^2-y^2}\rangle \pm i|d_{xy}\rangle$ provide the eigenstates with eigenvalues of orbital angular momentum (OAM) (see Supplemental Material [32] Sec. II). The double degeneracy in both E_1 and E_2 modes can be interpreted as a pseudo-Kramers pairing in the present PCs. Figure 1(c) also includes the 2D representations of the mode symmetries at the high-symmetry M and K points in the BZ for the two typical PCs defined in Fig. 1(b). As can be seen clearly in Fig. 1(d), a band inversion between E_1 and E_2 modes at the Γ point takes place as the ratio between the two competing lengths h_1/h_2 is swept, which indicates a topology phase transition (see Supplemental Material [32] Sec. II). The case of $h_1/h_2 = 1$, corresponding to a honeycomb lattice, is the phase transition point where the E_1 and E_2 modes are degenerate and Dirac cones appear in the frequency dispersion. This band inversion between p and d photonic modes with opposite spatial parities is the foundation of TRS topological states in the present dielectric photonic systems.

Because of the distinction in topology between the two PCs with inverted band properties, a pair of interface states appears, where the one with up pseudospin $|\sigma_z = +\rangle$, namely, positive (+) OAM, and that with down pseudospin $|\sigma_z = -\rangle$, namely, negative (−) OAM, propagate in opposite directions, very similar to the helical edge states in QSHE systems (see Supplemental Material [32] Sec. II). As a unique property of the present approach, unidirectional interface EM propagations can be excited, as will be shown in what follows.

We assemble two photonic crystals PC_1 and PC_2 with distinct topologies on the upper and lower side of the interface as shown in Fig. 1(a). The photonic band diagram calculated by COMSOL MULTIPHYSICS [39] is shown in Fig. 2(a), with the supercell including PC_1 and PC_2 displayed in the side panel. Over the whole system, we use the same alumina cylinders, a conventional dielectric material with relative dielectric permittivity $\varepsilon = 7.5$, with diameter $d = 6$ mm and the lattice constant $a = 25$ mm. The intra- and intercouple distances are taken as $h_1 = 0.36a$ and $h_2 = 0.28a$ in PC_1, whereas $h_1 = 0.30a$ and $h_2 = 0.40a$ in PC_2. The two pairs of competing lengths are taken in such a way that they satisfy the relation $h_1 > h_2$ and $h_1 < h_2$, respectively; thus, PC_1 and PC_2 are distinct in topology, and their photonic frequency gaps overlap with each other. As seen in Fig. 2(a), two topological interface states appear in the bulk band gap as highlighted by symbols. The distributions of the EM field obtained by an eigenmode analysis at the two points with opposite momenta [upward and downward triangles in Fig. 2(a)] are

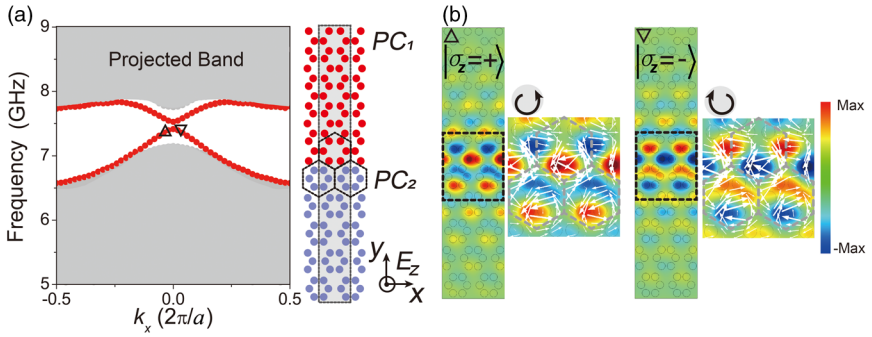

FIG. 2. (a) Calculated band diagram based on a supercell composed of PC_1 and PC_2 shown in the right panel, where a periodic (absorbing) boundary condition is applied on the x (y) direction, respectively. The folded bulk bands belonging to PC_1 or PC_2 are painted in gray, whereas the two topological interface bands are shown by symbols. (b) Distributions of the out-of-plane electric field (in gray levels, in color online) at the two opposite momenta denoted by the triangles in (a). The corresponding in-plane magnetic field is also displayed by arrows for the highlighted regions where the length of the arrow indicates the field strength. Black circular arrows indicate that the magnetic field rotates either counterclockwise or clockwise at the two opposite momenta.

displayed in Fig. 2(b). It is clear that the in-plane magnetic field rotates counterclockwise and clockwise for the two opposite momenta, respectively, corresponding to the two pseudospin states $|\sigma_z = +\rangle$ and $|\sigma_z = -\rangle$. While there is a small frequency gap in the dispersions of interface states in Fig. 2(a), the pseudospin is preserved and backscatterings are significantly suppressed as shown experimentally below.

Experimental verification of unidirectional waveguide.—In order to verify the momentum-pseudospin locking experimentally in a clear way, we design a four-antenna array to generate EM waves coupling with the interface modes carrying pseudospin $|\sigma_z = +\rangle/|\sigma_z = -\rangle$ (see Supplemental Material [32] Sec. III). As highlighted in the inset in Fig. 1(a), the antenna array is located on the interface of PC_1 and PC_2 [at the position $x = y = 0$ in Fig. 3(a)]. Because the EM modes with an electric field parallel to the cylinder axis are explored, a parallel-plate metallic waveguide setup is used to largely decrease the height of cylinders, and the time-harmonic out-of-plane electric-field distributions are measured with a probing antenna inside. Absorbing materials [in dark blue (online) in Fig. 1(a)] are arranged around the sample in the lateral directions. An Agilent E5071C vector network analyzer is used for data acquisition. The experimental visualization of the topological interface mode with up pseudospin $|\sigma_z = +\rangle$ is illustrated in Fig. 3(a) at 7.42 GHz, where the out-of-plane electric field is much enhanced in the rightward direction. We have measured quantitatively the distribution of the out-of-plane electric field along the whole interface and show the result obtained at $x =$ 100 mm in the upper panel in Fig. 3(c) as an example. The strength of the electric field decays into PC_1 and PC_2 with a decay length of 47.2 ± 7.8 and 43.7 ± 3.8 mm, respectively, indicating that the unidirectional EM propagation is confined well within a couple of unit cells of PC structures. A similar result was obtained at a single point on the interface in a previous work [25].

We evaluate the transmission in the two directions by evaluating the line integral of the measured profile of electric-field intensity as the frequency is swept. The resultant transmissions to the two ends $S1$ and $S2$ as indicated by the dashed lines in Fig. 3(a) are displayed in Fig. 3(b). Three different frequency regions can be identified. Region I (from 7.40 to 7.56 GHz) corresponds to the frequency range within the common band gap between PC_1 and PC_2. The transmission in the rightward direction ($S1$) is

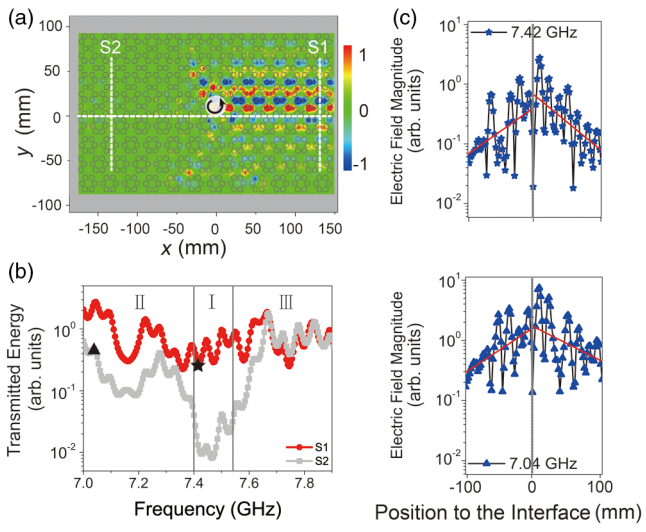

FIG. 3. (a) Experimentally measured distributions of the out-of-plane electric field at 7.42 GHz [indicated by the star in (b)] where an antenna array with positive OAM (represented by a counterclockwise circular arrow) is used to excite the $|\sigma_z = +\rangle$ state. (b) Measured transmissions to the two ends $S1$ and $S2$ of the sample. (c) Profiles of the magnitude of the out-of-plane electric field along the y direction at $x = 100$ mm away from the source at 7.42 (upper panel) and 7.04 GHz (lower panel) indicated by the star and triangle in (b), respectively. Magnitudes of the electric field are normalized to the incident field. The absorbing materials in experiments are indicated in gray.

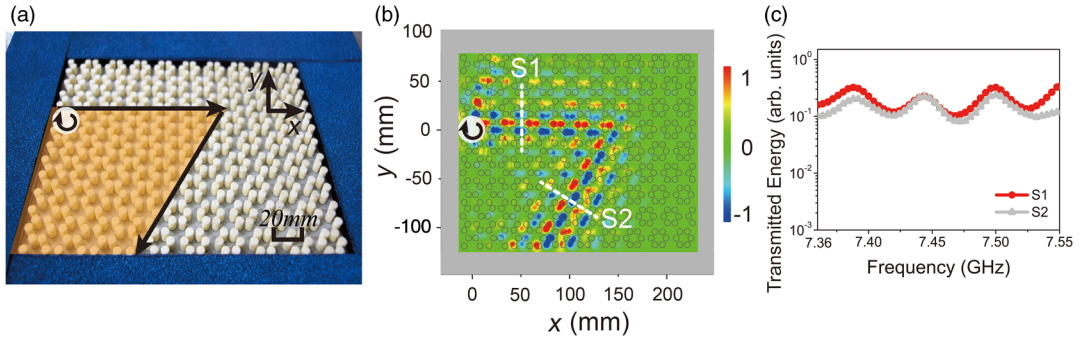

FIG. 4. (a) Photo of the experimental setup for the system with a 120° sharp turn in the interface between PC_1 (highlighted in gray, orange online) and PC_2, where the $|\sigma_z = -\rangle$ state is excited by a four-antenna array as indicated by a clockwise circular arrow. (b) Measured distribution of the out-of-plane electric field at frequency 7.41 GHz. (c) Measured transmissions to $S1$ and $S2$ as indicated in (b) by the dashed lines.

larger than that in the leftward direction ($S2$) by over one order of magnitude, indicating that a good isolation ratio is achieved. In this frequency region, the EM wave is well confined in the interfacial region, as typically shown in Figs. 3(a) and 3(c). The small frequency gap in the calculated dispersions of interface states [see Fig. 2(a)] is unnoticeable in our experiments. In region II, where the frequency is below the bulk band edge around 7.40 GHz, the interface state gradually approaches the continuum of bulk photonic bands of PC_1 and PC_2 as the frequency decreases, where the influence from the bulk modes is enhanced. Transmission in the two opposite directions increases simultaneously, and their difference gradually decreases upon a decreasing frequency. This observation provides a proof that our antenna with the given pseudospin does not emit EM waves in any preferred direction, and thus the unidirectional propagation shown in Fig. 3(a) is purely of topology origin. The effect can also be seen in the field distributions. As shown in Fig. 3(c) for $x = 100$ mm and 7.04 GHz, while the out-of-plane electric field is much stronger as compared to at 7.42 GHz, indicating that a certain number of bulk modes in PC_1 and PC_2 are excited, the interface state still survives, since the field magnitude is maximal at the interface and decays into both PCs. In frequency region III, starting from 7.56 GHz where the frequency is above the upper bulk band edge, the interface state is influenced strongly by the bulk photonic bands. We notice that in region III the group velocity of the interface mode is very small and even reverses its sign away from the Γ point, as can be seen in Fig. 2(a). The measured transmissions in the two directions quickly become comparable. We thus demonstrated a momentum-pseudospin locked interface mode in a TRS system that is associated with the topology of PC and is well confined to the interface.

In order to verify the effectiveness of the pseudospin design and the backscattering-immune property of the topological microwave channel created, we built a sharp turn of 120° along the interface as displayed in Fig. 4(a). The region of PC_1 structure is highlighted in light gray (in orange online), whereas the remaining region is of PC_2 structure, with the upper-lower arrangement opposite to those in Figs. 1 and 3. The antenna array is now designed to excite the $|\sigma_z = -\rangle$ pseudospin state. As can be seen in the measured electric-field distribution at the frequency of 7.41 GHz shown in Fig. 4(b), even though the total propagation length is nearly 3 times that as given in Fig. 3(a), and, moreover, a 120° sharp turn exists on the interface, the field magnitude of the interface state remains unchanged at the exit port. The transmission obtained from field-intensity integration at $S2$ is almost identical to that at the position $S1$ close to the source as shown in Fig. 4(c), indicating that the topological interface state with the desired pseudospin propagates without noticeable back-scattering from the sharp turn.

Discussions.—In the present experimental setup, the alumina cylinders are contained in the axial direction by two parallel metallic plates. This setup is adopted in order to reduce largely the height of dielectric cylinders, which makes experimental measurements much easier while leaving the topological physics designed for the TM mode intact where the electric field is finite only along the axial direction. It has been shown experimentally that the zero-index properties in dielectric PCs contained in metallic plates [40], the same geometry as used in the present work, were successfully extended to infrared frequencies [41] when sizes in lateral directions are scaled down and the sample height along the axial direction is sufficiently large with the open boundary condition. Therefore, the topological EM properties demonstrated in the present work in the microwave frequencies can be transferred to the near-infrared or even optical frequencies with the identical underlying physics.

The honeycomb structure has also been explored for achieving interface channels protected by the valley index [30,42–45]. In order to distinguish the present topological PC from a valley PC, we consider another type of interface including sharp turns of 90°. As shown in Fig. 5(a) for the field distributions obtained by finite-element simulations

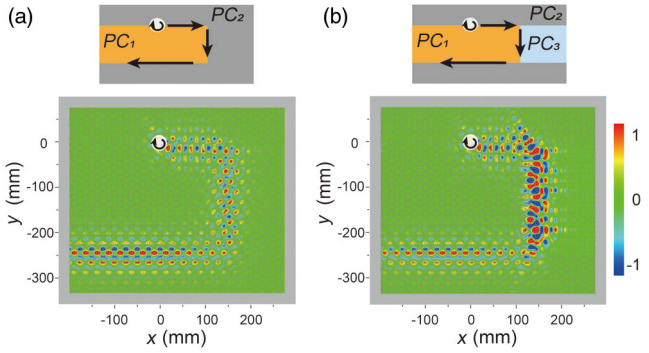

FIG. 5. (a) Simulated unidirectional propagation of the $|\sigma_z = -\rangle$ state at 6.69 GHz along the interface with 90° turns shown schematically in the upper panel. (b) Simulated unidirectional propagation with the same setup as (a) except that a photonic-insulating square-latticed PC_3 is included as a part of the interface to PC_1 as shown schematically in the upper panel.

[39], the $|\sigma_z = -\rangle$ interface state launched by a source at 6.69 GHz propagates along the interface with 90° turns without noticeable scattering, which cannot be expected for a valley PC. A topologically trivial PC_3 with a square lattice is also considered as shown schematically in the upper panel in Fig. 5(b), which is designed in such a way that its photonic band gap is overlapping with those of PC_1 and PC_2 (for details, see Supplemental Material [32] Sec. IV). It is clear that a stable EM pathway exists only along the interface between topological and trivial PCs, which indicates that a genuine topological photonic interface state is realized in our system.

While in the present work we have concentrated on topological photonic band engineering, other approaches have also been proposed to realize unidirectional propagations of EM waves towards the common goal of achieving one-way optic devices. It was discussed theoretically [46] that one-way propagation of circularly polarized modes can be achieved in a straight magnetoelectric chain or even in dielectric fine-tuned structures. Other approaches include a desired circular polarized microwave propagation in a three-dimensional PC with a chiral photonic band gap [47], a directional circular dipole emission in PC waveguides [48], and engineering PC waveguide dispersion to accommodate a highly directive chiral photon-emitter coupling [49].

In conclusion, unidirectional backscattering-immune photonic pathways with topological protection are demonstrated experimentally in microwave experiments using dielectric materials with time-reversal symmetry. The electromagnetic counterpart of the Kramers pair of electrons is achieved in the photonic crystal purely based on the geometric effect of honeycomb structures, and pseudospin-polarized electromagnetic waves with a given orbital angular momentum are selectively excited by a designed antenna array. The transversely confined and longitudinally directional interface propagation of the pseudospin-polarized electromagnetic state is visualized qualitatively and measured quantitatively. The electromagnetic properties demonstrated here are readily available at near-infrared or even optical frequencies upon scaling down the physical sizes, which are then expected to contribute to future optical communications. The present work demonstrates another example that the physics of topology can provide novel designs for future optical science and applications [50–52].

The work in Soochow University is supported by the National Natural Science Foundation of China (Grants No. 11574226 and No. 11675116), the Natural Science Foundation of Jiangsu Province (Grant No. BK20170058), and a project funded by the Priority Academic Program Development of Jiangsu Higher Education Institutions (PAPD). X. H. is supported by the WPI Initiative on Materials Nanoarchitectonics, Ministry of Education, Cultures, Sports, Science and Technology, Japan, and Grants-in-Aid for Scientific Research No. 17H02913, Japan Society for Promotion of Science.

*Corresponding author.
hu.xiao@nims.go.jp
†Corresponding author.
zhhang@suda.edu.cn

[1] K. V. Klitzing, G. Dorda, and M. Pepper, New Method for High-Accuracy Determination of the Fine Structure Constant Based on Quantized Hall Resistance, Phys. Rev. Lett. **45**, 494 (1980).
[2] D. J. Thouless, M. Kohmoto, M. P. Nightingale, and M. den Nijs, Quantized Hall Conductance in a Two-Dimensional Periodic Potential, Phys. Rev. Lett. **49**, 405 (1982).
[3] F. D. M. Haldane, Model for a Quantum Hall Effect without Landau Levels: Condensed-Matter Realization of the "Parity Anomaly", Phys. Rev. Lett. **61**, 2015 (1988).
[4] C. L. Kane and E. J. Mele, Quantum Spin Hall Effect in Graphene, Phys. Rev. Lett. **95**, 226801 (2005).
[5] B. A. Bernevig, T. L. Hughes, and S. C. Zhang, Quantum spin Hall effect and topological phase transition in HgTe quantum wells, Science **314**, 1757 (2006).
[6] M. König, S. Wiedmann, C. Brüne, A. Roth, H. Buhmann, L. W. Molenkamp, X.-L. Qi, and S.-C. Zhang, Quantum spin Hall insulator state in HgTe quantum wells, Science **318**, 766 (2007).
[7] M. Z. Hasan and C. L. Kane, Colloquium: Topological insulators, Rev. Mod. Phys. **82**, 3045 (2010).
[8] X.-L. Qi and S.-C. Zhang, Topological insulators and superconductors, Rev. Mod. Phys. **83**, 1057 (2011).
[9] H.-M. Weng, R. Yu, X. Hu, X. Dai, and Z. Fang, Quantum anomalous Hall effect and related topological electronic states, Adv. Phys. **64**, 227 (2015).
[10] F. D. M. Haldane and S. Raghu, Possible Realization of Directional Optical Waveguides in Photonic Crystals with Broken Time-Reversal symmetry, Phys. Rev. Lett. **100**, 013904 (2008).

[11] Z. Wang, Y. Chong, J. D. Joannopoulos, and M. Soljačić, Observation of unidirectional backscattering immune topological electromagnetic states, Nature (London) **461**, 772 (2009).
[12] Y. Poo, R. Wu, Z. Lin, Y. Yang, and C. T. Chan, Experimental Realization of Self-Guiding Unidirectional Electromagnetic Edge States, Phys. Rev. Lett. **106**, 093903 (2011).
[13] S. Skirlo, L. Lu, Y. Igarashi, Q. Yan, J. D. Joannopoulos, and M. Soljačić, Experimental Observation of Large Chern Numbers in Photonic Crystals, Phys. Rev. Lett. **115**, 253901 (2015).
[14] M. C. Rechtsman, J. M. Zeuner, Y. Plotnik, Y. Lumer, D. Podolsky, F. Dreisow, S. Nolte, M. Segev, and A. Szameit, Photonic Floquet topological insulators, Nature (London) **496**, 196 (2013).
[15] J. J. Sakurai, *Modern Quantum Mechanics*, revised ed. (Addison-Wesley, Reading, MA, 1993).
[16] L. Lu, J. D. Joannopoulos, and M. Soljačić, Topological states in photonic systems, Nat. Phys. **12**, 626 (2016).
[17] A. B. Khanikaev, Photonic topological insulators, Nat. Mater. **12**, 233 (2013).
[18] C. He, X.-C. Sun, X.-P. Liu, M.-H. Lu, Y. Chen, L. Feng, and Y.-F. Chen, Photonic topological insulator with broken time-reversal symmetry, Proc. Natl Acad. Sci. U.S.A. **113**, 4924 (2016).
[19] M. Hafezi, E. A. Demler, M. D. Lukin, and J. M. Taylor, Robust optical delay lines with topological protection, Nat. Phys. **7**, 907 (2011).
[20] M. Hafezi, S. Mittal, J. Fan, A. Migdall, and J. M. Taylor, Imaging topological edge states in silicon photonics, Nat. Photonics **7**, 1001 (2013).
[21] K. Fang, Z. Yu, and S. Fan, Realizing effective magnetic field for photons by controlling the phase of dynamic modulation, Nat. Photonics **6**, 782 (2012).
[22] M. C. Rechtsman, J. M. Zeuner, A. Tünnermann, S. Nolte, M. Segev, and A. Szameit, Strain-induced pseudomagnetic field and photonic Landau levels in dielectric structures, Nat. Photonics **7**, 153 (2013).
[23] L. D. Tzuang, K. Fang, P. Nussenzveig, S. Fan, and M. Lipson, Non-reciprocal phase shift induced by an effective magnetic flux for light, Nat. Photonics **8**, 701 (2014).
[24] W.-J. Chen, S.-J. Jiang, X.-D. Chen, B. Zhu, L. Zhou, J.-W. Dong, and C. T. Chan, Experimental realization of photonic topological insulator in a uniaxial metacrystal waveguide, Nat. Commun. **5**, 5782 (2014).
[25] X. Cheng, C. Jouvaud, X. Ni, S. H. Mousavi, A. Z. Genack, and A. B. Khanikaev, Robust reconfigurable electromagnetic pathways within a photonic topological insulator, Nat. Mater. **15**, 542 (2016).
[26] J. D. Joannopoulos, S. G. Johnson, J. N. Winn, and R. D. Meade, *Photonic Crystals: Molding the Flow of Light*, 2nd ed. (Princeton University, Princeton, NJ, 2008).
[27] L.-H. Wu and X. Hu, Scheme for Achieving a Topological Photonic Crystal by Using Dielectric Material, Phys. Rev. Lett. **114**, 223901 (2015).
[28] C. He, X. Ni, H. Ge, X.-C. Sun, Y.-B. Chen, M.-H. Lu, X.-P. Liu, and Y.-F. Chen, Acoustic topological insulator and robust one-way sound transport, Nat. Phys. **12**, 1124 (2016).
[29] S. Yves, R. Fleury, T. Berthelot, M. Fink, F. Lemoult, and G. Lerosey, Crystalline metamaterials for topological properties at subwavelength scales, Nat. Commun. **8**, 16023 (2017).
[30] T. Ma and G. Shvets, All-Si valley-Hall photonic topological insulator, New J. Phys. **18**, 025012 (2016).
[31] S. Barik, H. Miyake, W. DeGottardi, E. Waks, and M. Hafezi, Two-dimensionally confined topological edge states in photonic crystals, New J. Phys. **18**, 113013 (2016).
[32] See Supplemental Material at http://link.aps.org/supplemental/10.1103/PhysRevLett.120.217401, for the details of doubly degenerate Dirac cone dispersion, pseudospin construction and theoretical analysis, experimental realization of source, and rectangle interface geometry, which includes Refs. [33–37].
[33] S. Raghu and F. D. M. Haldane, Analogs of quantum-Hall-effect edge states in photonic crystals, Phys. Rev. A **78**, 033834 (2008).
[34] B. A. Bernevig and T. L. Hughes, *Topological Insulators and Topological Superconductors* (Princeton University, Princeton, NJ, 2013).
[35] L. Xu, H.-X. Wang, Y. Xu, H. Chen, and J.-H. Jiang, Accidental degeneracy in photonic bands and topological phase transitions in two-dimensional core-shell dielectric photonic crystals, Opt. Express **24**, 18059 (2016).
[36] H.-X. Wang, L. Xu, H. Chen, and J.-H. Jiang, Three-dimensional photonic Dirac points stabilized by point group symmetry, Phys. Rev. B **93**, 235155 (2016).
[37] L.-H. Wu and X. Hu, Topological properties of electrons in honeycomb lattice with detuned hopping energy, Sci. Rep. **6**, 24347 (2016).
[38] K. Sakoda, *Optical Properties of Photonic Crystals*, 2nd ed. (Springer Science & Business Media, Berlin, 2005).
[39] COMSOL MULTIPHYSICS 4.3a, rf module, commercial software based on the finite-element method (http://www.comsol.com).
[40] X. Q. Huang, Y. Lai, Z. H. Hang, H. H. Zheng, and C. T. Chan, Dirac cones induced by accidental degeneracy in photonic crystals and zero-refractive-index materials, Nat. Mater. **10**, 582 (2011).
[41] P. Moitra, Y. Yang, Z. Anderson, I. I. Kravchenko, D. P. Briggs, and J. Valentine, Realization of an all-dielectric zero-index optical metamaterial, Nat. Photonics **7**, 791 (2013).
[42] A. Rycerz, J. Tworzydło, and C. W. J. Beenakker, Valley filter and valley valve in graphene, Nat. Phys. **3**, 172 (2007).
[43] L. Ju, Z. Shi, N. Nair, Y. Lv, C. Jin, J. V. Jr, C. Ojeda-Aristizabal, H. A. Bechtel, M. C. Martin, A. Zettl, J. Analytis, and F. Wang, Topological valley transport at bilayer graphene domain walls, Nature (London) **520**, 650 (2015).
[44] J. Lu, C. Qiu, L. Ye, X. Fan, M. Ke, F. Zhang, and Z. Liu, Observation of topological valley transport of sound in sonic crystals, Nat. Phys. **13**, 369 (2017).
[45] X. Wu, Y. Meng, J. Tian, Y. Huang, H. Xiang, D. Han, and W. Wen, Direct observation of valley-polarized topological edge states in designer surface plasmon crystals, Nat. Commun. **8**, 1304 (2017).
[46] Y. Mazor and B. Z. Steinberg, Modal and excitation asymmetries in magnetodielectric particle chains, Phys. Rev. B **94**, 235114 (2016).

[47] W.-J. Chen, Z. H. Hang, J.-W. Dong, X. Xiao, H.-Z. Wang, and C. T. Chan, Observation of Backscattering-Immune Chiral Electromagnetic Modes without Time Reversal Breaking, Phys. Rev. Lett. **107**, 023901 (2011).

[48] B. le Feber, N. Rotenber, and L. Kuipers, Nanophotonic control of circular dipole emission, Nat. Commun. **6**, 6695 (2015).

[49] I. Söllner, S. Mahmoodian, S. L. Hansen, L. Midolo, A. Javadi, G. Kiršanskė, T. Pregnolato, H. El-Ella, E. H. Lee, J. D. Song, S. Stobbe, and P. Lodahl, Deterministic photon-emitter coupling in chiral photonic circuits, Nat. Nanotechnol. **10**, 775 (2015).

[50] B. Bahari, A. Ndao, F. Vallini, A. E. Amili, Y. Fainman, and B. Kanté, Nonreciprocal lasing in topological cavities of arbitrary geometries, Science **358**, 636 (2017).

[51] A. Slobozhanyuk, A. V. Shchelokova, X. Ni, S. H. Mousavi, D. A. Smirnova, P. A. Belov, A. Alù, Y. S. Kivshar, and A. B. Khanikaev, Near-field imaging of spin-locked edge states in all-dielectric topological metasurfaces, arXiv: 1705.07841.

[52] S. Barik, A. Karasahin, C. Flower, T. Cai, H. Miyake, W. DeGottardi, M. Hafezi, and E. Waks, A topological quantum optics interface, Science **359**, 666 (2018).